Acceleration of proton bunches by petawatt chirped radially polarized laser pulses

Jian-Xing Li,[1,*] Yousef I. Salamin,[1,2] Benjamin J. Galow,[1] and Christoph H. Keitel[1]
[1]*Max-Planck-Institut für Kernphysik, Saupfercheckweg 1, D-69029 Heidelberg, Germany*
[2]*Department of Physics, American University of Sharjah, POB 26666, Sharjah, United Arab Emirates*
(Received 13 March 2012; published 25 June 2012)

Results from theoretical investigations are presented which show that protons can be accelerated from rest to a few hundred MeV by a 1-PW chirped radially polarized laser pulse of several hundred femtosecond duration and focused to a waist radius comparable to the radiation wavelength. Single-particle calculations are supported by many-particle and particle-in-cell simulations. Compared with laser acceleration by a similar linearly polarized pulse, the gained energies are less, but have better beam quality. For a suitable initial phase, a particle bunch gets accelerated by the axial component E_z of the laser pulse and, initially focused by the transverse electric field component E_r. Beam diffraction finally sets in due to the particle-particle Coulomb repulsion, after interaction with the pulse ceases to exist.

DOI: 10.1103/PhysRevA.85.063832 PACS number(s): 37.20.+j, 37.10.Vz, 52.38.Kd, 42.65.−k

I. INTRODUCTION

Radially polarized light has several unique features that qualify it for a number of important applications. It is well known that a radially polarized laser beam can be focused to a smaller waist radius than is possible for a linearly polarized one, and that focusing results in concentrating much of the energy of the beam in a needlelike axial focus [1–4]. The fact that the radial component of the electric field vanishes on the beam axis, makes the strong axial component ideal for utilization in such industrial applications as lithography [5], material processing [6], high-resolution microscopy [7,8], and particle trapping and acceleration [9–13].

Several intracavity and extracavity techniques have been used for generating radially polarized light [14–18]. Unfortunately, only radially polarized systems of modest power can be generated using these techniques. In fact, the maximum power reached so far does not exceed 3 kW [19,20], although the much higher powers of 580 MW [21] and 1 TW [22], produced by passing a CO_2 laser beam through an axicon, have been mentioned in connection with particle laser acceleration.

Our interest, in the present work, is in laser acceleration of protons by means of a chirped, radially polarized, pulse. Only electron laser acceleration using chirped radially polarized light has recently been studied theoretically [23–28]. On the other hand, proton acceleration by chirped, linearly polarized laser pulses has been the subject of recent theoretical investigations [29,30].

In this paper, we are interested in laser acceleration of protons to several hundred MeV, an application that requires extremely powerful systems, capable of delivering ultrahigh intensities when focused to micron-size spatial dimensions. Earlier work [9,10,31], utilizing unchirped laser light of the radially polarized variety, has demonstrated the need for $\sim$10 PW powers, intensities in excess of $>10^{23}$ W/cm^2, and focusing to subwavelength waist radii. Single-particle calculations, supported by many-particle and particle-in-cell (PIC) simulations, will be shown here to lead to the need for only $\simeq$1 PW peak-power laser pulses, of peak intensities of the order of $\simeq 10^{22}$ W/cm^2, and focused to waist radii w_0 of the order of one laser wavelength λ_0, provided the laser pulses are properly chirped.

Proton laser acceleration, by irradiating metal targets by unchirped pulses, has been the subject of theoretical and experimental investigation for quite some time now. For thin target foils, the mechanism at work is the target normal sheath acceleration (TNSA) [32–39]. On the other hand, it is now believed that ions get accelerated, from an ultrathin target irradiated by an ultraintense beam, by the radiation pressure acceleration (PRA) mechanism [40–44]. For mass-limited targets which have typically spatial dimensions of the order of the laser wavelength we refer to Refs. [45–47]. In acceleration by a chirped laser pulse, subject of the present paper, the underlying mechanism will be shown to be particle-field synchronization, brought about by symmetry breaking of the pulse due to the frequency chirp [25–30,48,49].

In Sec. II, fields of a chirped radially polarized laser pulse will be described in terms of those of a continuous beam multiplied by a Gaussian carrier envelope. Introduction of the linear frequency chirp, and the propagation of its effect to the remaining pulse parameters, will be done in the same section. The single-particle calculations will be described, and their results discussed, in Sec. III. It will be shown there that a proton can gain a few hundred MeV from interaction with 1-PW upchirped and downchirped, 150-fs pulses, focused down to $w_0 = \lambda_0$ waist radii. Section IV will be devoted to the many-particle calculations. There, initial ensembles of 3000 protons will be shown to be accelerated to mean energies of a few hundred MeV, by pulses similar to those used in Sec. III. These results will be supported by 2D3V PIC simulations, to be described in Sec. V. Such simulations are necessary for handling the initial plasma formed when the laser pulse ionizes the target, a hydrogen gas jet or an expanding hydrogen cluster, employed as a source of the protons. A general discussion of our main findings will be conducted in Sec. VI.

II. THE FIELDS

The electric field components E_r and E_z, and the magnetic field component B_θ, of the radially polarized pulse will be

[*]J.X.L. is on leave from the College of Physics Science and Information Engineering, Hebei Normal University, Shijiazhuang 050016, China.

modeled using those of continuous-wave (cw) Gaussian-beam-based expressions, multiplied by the Gaussian pulse carrier envelope,

$$g(\eta) = e^{-\eta^2/2\sigma^2}; \quad \sigma = \frac{\Delta\eta}{2\sqrt{2\ln 2}}. \tag{1}$$

In Eq. (1) $\eta = \omega_0(t - z/c)$, where ω_0 is the laser frequency, t is the time, z is the coordinate along the direction of propagation, and c is the speed of light in vacuum. Furthermore, σ is given in terms of the full width at half maximum $\Delta\eta$ of the envelope in η space. The latter, in turn, is given in terms of the temporal full width at half maximum τ of the pulse by $\Delta\eta \simeq \omega_0\tau$. For the CW fields, the generalized Lax series expressions will be adopted to order $O(\varepsilon^4)$, where ε is the diffraction angle, defined as the ratio of the beam's radius at focus w_0 to the Rayleigh length $z_r = \pi w_0^2/\lambda_0$. To make this work as self-contained as possible, the field components are quoted here from Ref. [50] as

$$E_r = E\left\{\varepsilon\rho C_2 + \varepsilon^3\left[-\frac{\rho C_3}{2} + \rho^3 C_4 - \frac{\rho^5 C_5}{4}\right]\right\}, \tag{2}$$

$$E_z = E\left\{\varepsilon^2[S_2 - \rho^2 S_3] + \varepsilon^4\left[\frac{S_3}{2} + \frac{\rho^2 S_4}{2} - \frac{5\rho^4 S_5}{4} + \frac{\rho^6 S_6}{4}\right]\right\}, \tag{3}$$

$$B_\theta = \frac{E}{c}\left\{\varepsilon\rho C_2 + \varepsilon^3\left[\frac{\rho C_3}{2} + \frac{\rho^3 C_4}{2} - \frac{\rho^5 C_5}{4}\right]\right\}. \tag{4}$$

The symbols in Eqs. (2)–(4) have the following definitions:

$$E = E_0 e^{-r^2/w^2}; \quad w = w_0\sqrt{1+\zeta^2}, \tag{5}$$

$$C_n = \left(\frac{w_0}{w}\right)^n \cos(\psi + n\psi_G); \quad n = 2,3,\ldots,6. \tag{6}$$

$$S_n = \left(\frac{w_0}{w}\right)^n \sin(\psi + n\psi_G), \tag{7}$$

where $\rho = r/w_0$, $r = \sqrt{x^2+y^2}$, $\psi_G = \tan^{-1}\zeta$ is the Guoy phase, and $\zeta = z/z_r$. Furthermore,

$$\psi = \psi_0 + \omega t - k_0 z - \frac{k_0 r^2}{2R}; \quad R = z + \frac{z_r^2}{z}, \tag{8}$$

with ψ_0 a *constant* initial phase, and $k_0 = 2\pi/\lambda_0$ the wave number. The expressions above contain only one term each above the often used paraxial approximation. In all of the cases to be discussed in the subsequent sections, our calculations show that dropping terms in the series of order $O(\varepsilon^5)$ and beyond, does not appreciably affect the results obtained.

To the same order in ε, the input power of the radially polarized beam will be quoted here for future reference, as

$$P_0 = \frac{\pi w_0^2}{2}\frac{E_0^2}{c\mu_0}\left(\frac{\varepsilon}{2}\right)^2\left[1 + 3\left(\frac{\varepsilon}{2}\right)^2\right], \tag{9}$$

where μ_0 is the permeability of free space and E_0 is a constant amplitude. The input (or peak) power has been calculated, as usual, from integrating the Poynting vector over the entire plane through the focus and perpendicular to the direction of propagation. Recall that [51], in the paraxial approximation, the beam intensity peaks at points in this plane on a circle of radius $r = w_0/\sqrt{2}$. For our purposes in this work, intensity at these points will be taken as the *peak intensity* I_0. In terms of the peak power given in Eq. (9) the peak intensity, attained at points in the focal plane with coordinates $r = w_0/\sqrt{2}$, is

$$I_0 = \left(\frac{2P_0}{\pi e w_0^2}\right)\left\{\frac{1 + \frac{3}{4}\varepsilon^2}{1 + \frac{5}{8}\varepsilon^2}\right\}, \tag{10}$$

where $e \simeq 2.7183$ is the base of the natural logarithm function ln.

The equations of motion will be turned into a set using the quantity $\eta = \omega_0(t - z/c)$ as a variable instead of the time t. The relationship between t and η is not simple, nor is it universal. It depends on the details of the particle trajectory through $z(\eta)$ or, equivalently, in terms of $z(t)$. Variation of some of the dynamical quantities to be discussed shortly will also be presented in terms of η. Examples include evolution of the particle's kinetic energy. The particle trajectories in real space will be represented parametrically in terms of η.

Chirping the frequency of the laser pulse will be introduced through replacing the (unchirped, or central) angular frequency ω_0 by

$$\omega_0(\eta) = \omega_0(1 + b\eta), \tag{11}$$

in which b is a dimensionless chirp parameter. The wavelength will be chirped as a direct result of chirping the frequency, that is,

$$\lambda(\eta) = \frac{2\pi c}{\omega(\eta)} = \frac{\lambda_0}{(1+b\eta)}, \tag{12}$$

from which also follows that the wave number,

$$k(\eta) = \frac{2\pi}{\lambda(\eta)} = k_0(1 + b\eta). \tag{13}$$

At this point, two assumptions will be made which will affect all of the subsequent developments, calculations, and final results and conclusions. First, the input power will be assumed fixed, not to be altered by chirping. Second, the (unchirped) waist radius at focus will be written in terms of the (unchirped) wavelength as $w_0 = \alpha\lambda_0$, where α is a constant, not to be affected by chirping. The second assumption entails that the diffraction angle $\varepsilon = \lambda_0/(\pi w_0) = 1/(\pi\alpha)$ stays fixed, as well, but that the waist radius will be chirped, and given by

$$w_0(\eta) = \frac{w_0}{1 + b\eta}. \tag{14}$$

These results, together with the first assumption, lead to the conclusion that the field amplitude will also need to be replaced by the chirped form,

$$E_0(\eta) = E_0(1 + b\eta). \tag{15}$$

Equations (11)–(15) will be used to replace the corresponding unchirped quantities everywhere in the field expressions E_r, E_z, and B_θ. In terms of the Cartesian coordinates x, y, and z, the field components should also be properly transformed, namely by

$$E_x = E_r\cos\theta; \quad E_y = E_r\sin\theta, \tag{16}$$

$$B_x = -B_\theta\sin\theta; \quad B_y = B_\theta\cos\theta, \tag{17}$$

where $\theta = \tan^{-1}(y/x)$.

In the next three sections, results from numerical solutions to the particle's equations of motion, in the fields given by

Eqs. (2)–(4) and subject to well-defined initial conditions, will be presented and discussed. Single-particle solutions will be carried out first, followed by many-particle calculations, and finally particle-in-cell simulations will be performed. The initial phase ψ_0 of the pulse fields plays an important role in determining evolution of the particle dynamics. As it turns out, the choice of $\psi_0 = 0$ leads to E_r playing a decisive role in confining motion of the accelerated particles to regions close to the propagation direction, during interaction with the pulse. Since this is such a desirable feature, which results in limiting the spatial spreading of a beam of such particles, the choice of $\psi_0 = 0$ will be made throughout this paper.

III. SINGLE-PARTICLE CALCULATIONS

In this section, calculations pertaining to the motion of a single particle, of mass M and charge Q, initially at rest at the origin of coordinates and subjected to a radially polarized laser pulse incident left to right on it as shown in Fig. 1, will be carried out. The relativistic Newton-Lorentz equations of motion (energy-momentum transfer equations) of the particle in the fields described in Sec. II above, read

$$\frac{d\boldsymbol{p}}{dt} = Q(\boldsymbol{E} + c\boldsymbol{\beta} \times \boldsymbol{B}); \quad \frac{d\mathcal{E}}{dt} = Qc\boldsymbol{\beta} \cdot \boldsymbol{E}, \tag{18}$$

where $\boldsymbol{p} = \gamma Mc\boldsymbol{\beta}$ and $\mathcal{E} = \gamma Mc^2$ are the relativistic particle momentum and energy, respectively, $\boldsymbol{\beta}$ is the velocity scaled by c, and $\gamma = (1 - \beta^2)^{-1/2}$ is the Lorentz factor. Equation (18) may now be combined to yield

$$\frac{d\boldsymbol{\beta}}{dt} = \frac{Q}{\gamma Mc}\left[(\boldsymbol{E} + c\boldsymbol{\beta} \times \boldsymbol{B}) - \boldsymbol{\beta}(\boldsymbol{\beta} \cdot \boldsymbol{E})\right], \tag{19}$$

for the scaled velocity $\boldsymbol{\beta}$. For the tightly focused fields, Eq. (19) can only be solved numerically. Solutions that yield $\boldsymbol{\beta}$ may immediately be used to obtain the particle's Lorentz factor. The most important quantity for our purposes in this work, namely, the kinetic energy of the particle, will follow from

$$K = (\gamma - 1)Mc^2. \tag{20}$$

Other quantities, such as the particle momenta and trajectories, may, in principle, be obtained from the numerical solutions.

Attention will be focused here on the exit kinetic energy of the particle, K_{exit}, after it has been left behind the pulse. To have a sense of the values of the chirp parameter b that are required

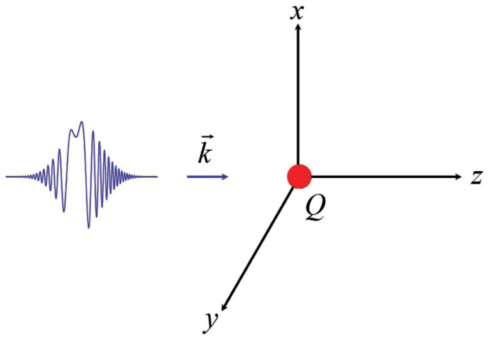

FIG. 1. (Color online) A schematic illustrating the initial conditions of the single-particle interaction with a chirped laser pulse.

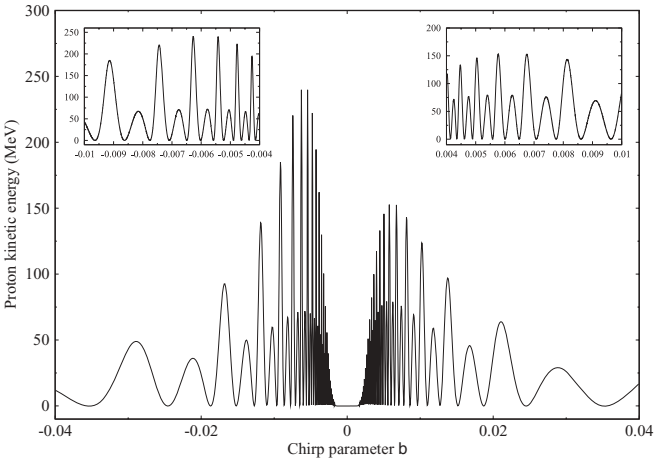

FIG. 2. Variation of the proton exit kinetic energy with the dimensionless parameter. The laser parameters used are as follows: $P_0 = 1$ PW, $w_0 = \lambda_0$, $I_0 \simeq 1.178 \times 10^{22}$ W/cm^2, $\tau = 150$ fs, and $\lambda_0 = 1$ μm. In the insets we zoom in on parts corresponding to the highest particle kinetic energies achievable for cases of downchirp (left) and upchirp (right).

for achieving the desired levels of acceleration, variation of K_{exit}, with positive (upchirp) as well as negative (downchirp) values of b, is shown in Fig. 2. For a small range of values around $b = 0$, one notes that there is essentially zero energy gain by the particle from the laser field, for the set of parameters employed. Elsewhere, the exit kinetic energy oscillates with b, exhibiting sharper peaks for small (absolute) values than for larger ones. This implies that dependence of the exit kinetic energy on the chirp parameter b is quite sensitive. A question may potentially arise as to whether the sensitive dependence upon b would lead to problems in experimental realization of the scheme. To answer this question, it should be recalled that b has been introduced as a parameter to model a pulse shape having broken symmetry, which results in substantial energy gain (as will be seen shortly). Experimentally, every pulse is uniquely defined by its spectrum. Hence, to generate such a pulse, one ought to synthesize it by its particular spectrum. Due to the implicit meaning of b, we do not expect sensitive dependence of the theoretical model on b to hinder an experimental realization of the scheme.

The exit kinetic energies shown in Fig. 2 are less than would be obtained from a linearly polarized pulse of the same parameters and under similar conditions [29,30]. Advantages for using a radially polarized pulse, however, will be in the accelerated particle beam qualities of energy spread and focusing. These issues will be discussed further in the subsequent sections.

For further insight into the acceleration by the chirped pulse, evolution of the kinetic energy of a single particle with η (in essence, in both space and time) is shown in Fig. 3, for two values of b. The cases of $b = -0.006\,27$ and $b = +0.005\,77$ correspond to the global maxima on the left and right halves of the figure, respectively. These maxima are $K_{\text{exit}} \simeq 242.7$ MeV and 154.4 MeV, respectively, as may roughly be read off Fig. 3(a). The normalized electric field components $E_z/E_0(\eta)$ sensed by the proton during interaction, in each case, are shown in Fig. 3(b). Note the correlation

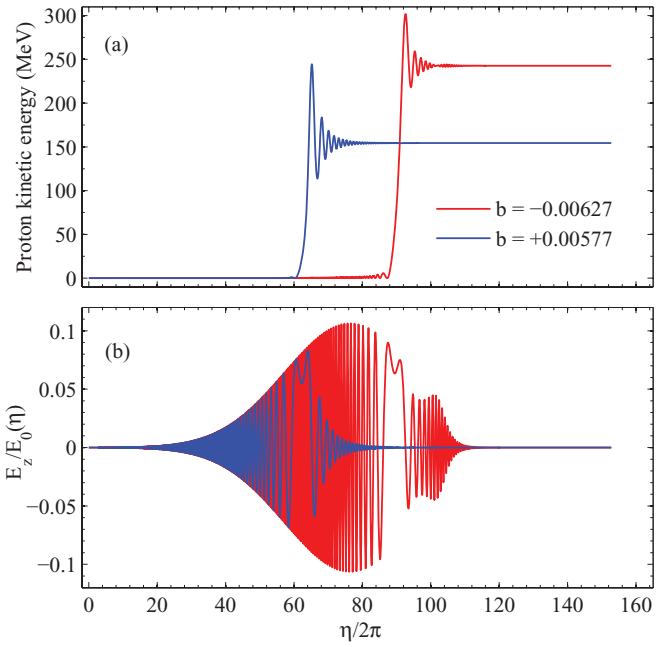

FIG. 3. (Color online) (a) Single proton exit kinetic energy evolution with space time (through η) for two values of the dimensionless chirp parameter. (b) The electric field component E_z, normalized by $E_0(\eta)$, sensed in flight by protons whose kinetic energy evolutions are shown in (a). All other parameters are the same as in Fig. 2.

between the corresponding lines shown in Figs. 3(a) and 3(b). Interaction with the quasistatic parts of the fields results in a substantial rise in the particle's kinetic energy, while interaction with the oscillatory parts leads to little gain, if at all. The quasistatic part of the field hints at the existence of a zero-frequency component in the spectrum of the pulse, but, it has been demonstrated recently [30] that a small band of frequencies, centered on the zero frequency, may be filtered out of the spectrum without lowering the exit kinetic energy calculated employing the laser pulse model.

In practical applications the particle trajectory is of paramount importance. The need to deliver the accelerated proton, say to the tumor of a patient in an ion therapy unit, requires knowledge of its trajectory with utmost precision. Starting from a position of rest near the origin, a single particle

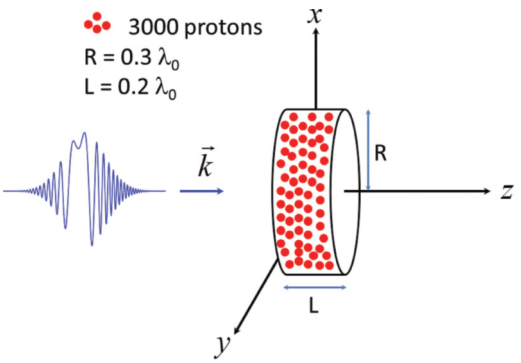

FIG. 4. (Color online) A schematic illustrating the initial conditions for an ensemble of 3000 noninteracting protons prior to interaction with a chirped laser pulse incident upon them from the left.

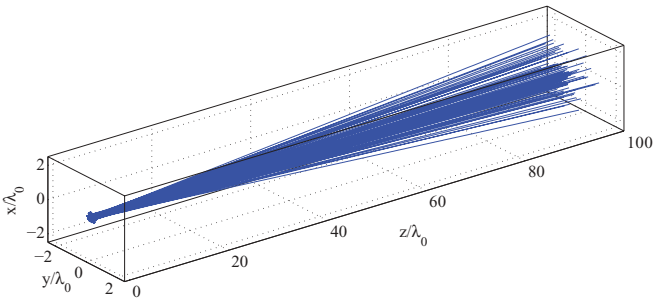

FIG. 5. (Color online) Three-dimensional (3D) trajectories of 100 protons, chosen at random from the initial ensemble of 3000 distributed uniformly within a disk of radius $0.3\lambda_0$ and thickness $0.2\lambda_0$ (see Fig. 4) as a result of interaction with a radially polarized laser pulse chirped at $b = -0.006\,27$. All other parameters are the same as in Fig. 2, and the interaction time corresponds to the interval from $\eta = 0$ to $\eta = 8\sigma$.

follows a trajectory dictated by the parameters of the pulse with which it interacts. This issue will be discussed further in the next section. The path followed by a particle which starts from a position of rest at the origin, however, is unique. Inspection of Eq. (2) shows that E_r vanishes identically for all points on the $z$axis, where $r = 0$. So, such a particle may initially move back and forth on the z axis for a while, but will finally be left behind the pulse to travel along z.

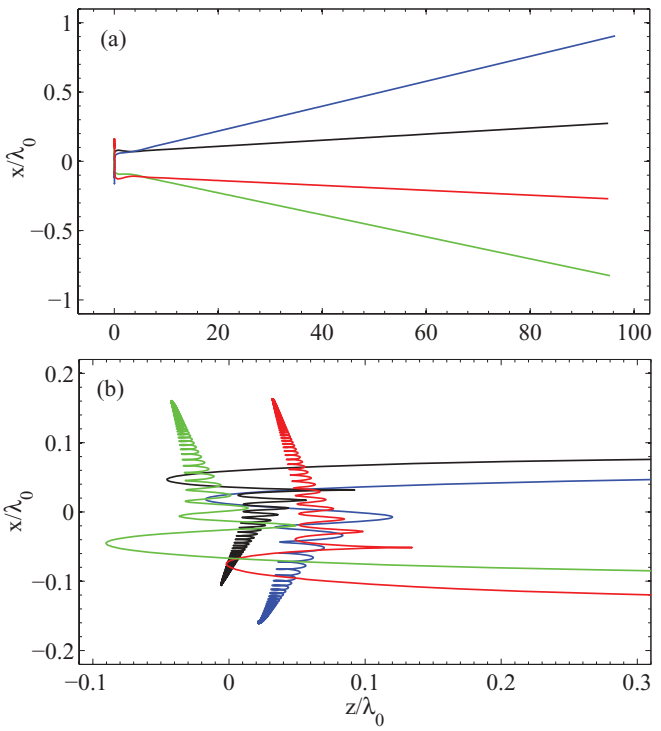

FIG. 6. (Color online) (a) Projections onto the xz plane of four single proton trajectories, all for the case of $b = -0.006\,27$. (b) A zoom in on the leftmost part of the trajectories shown in (a). The protons were chosen randomly from an ensemble that is described in Sec. IV. All other parameters are the same as in Fig. 2.

IV. MANY-PARTICLE CALCULATIONS

The assumption of initial position at the origin of coordinates, employed in the single-particle calculations so far, is quite idealistic. In practice, a more realistic assumption should take into account position fluctuations around the origin. On the other hand, one accelerates many particles for applications. To take care of both of these points, the dynamics of an ensemble of 3000, otherwise noninteracting, protons will be investigated in this section. The ensemble members all start from rest, but will be picked at random from initial positions within a cylinder (or disk) of height $L = 0.2\lambda_0$ and radius $R = 0.3\lambda_0$. The center of the ensemble will be assumed to start at the origin with the axis of its enclosing disk oriented along the pulse propagation direction, as shown in Fig. 4. Note that these data correspond to a particle density of

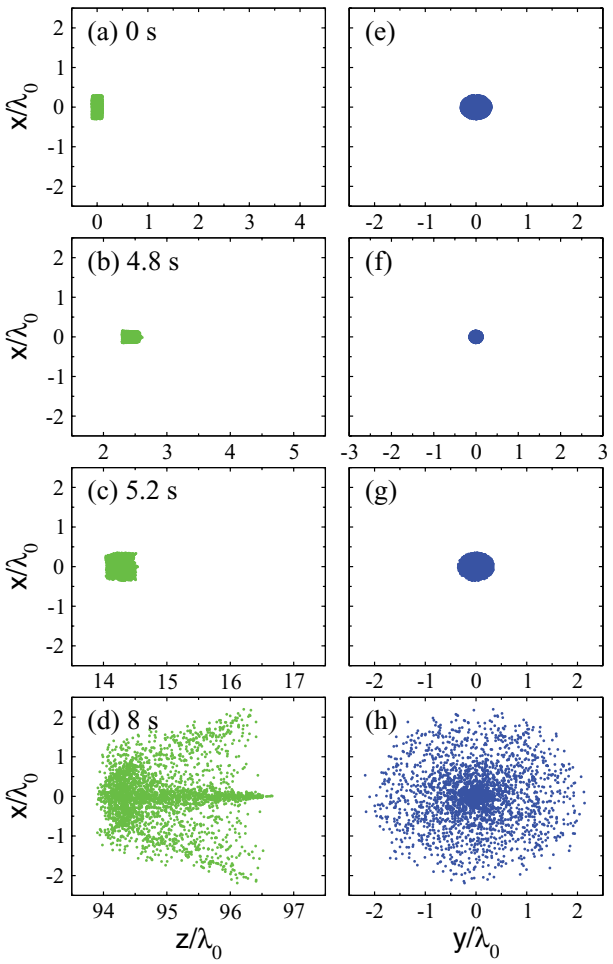

FIG. 7. (Color online) Evolution in η of an ensemble of 3000 protons, assumed to be noninteracting, initially at rest and randomly distributed within a cylinder of length $L = 0.2\lambda_0$, radius $R = 0.3\lambda_0$, centered at the origin of a Cartesian coordinate system and whose axis is oriented along z. (a)–(d) Snapshots of the projection of the evolving ensemble onto the xz plane; (e)–(h) snapshots of the projection onto the xy plane. Top to bottom, the pairs of snapshots are for times corresponding to η equal to 0, 4.8σ, 5.2σ, and 8σ, respectively. Note that $\eta = 0$ and $\eta = 8\sigma$ mark the start and end, respectively, of the particle-field interaction. The pulse parameters are the same as is Fig. 2 for $b = -0.006\,27$.

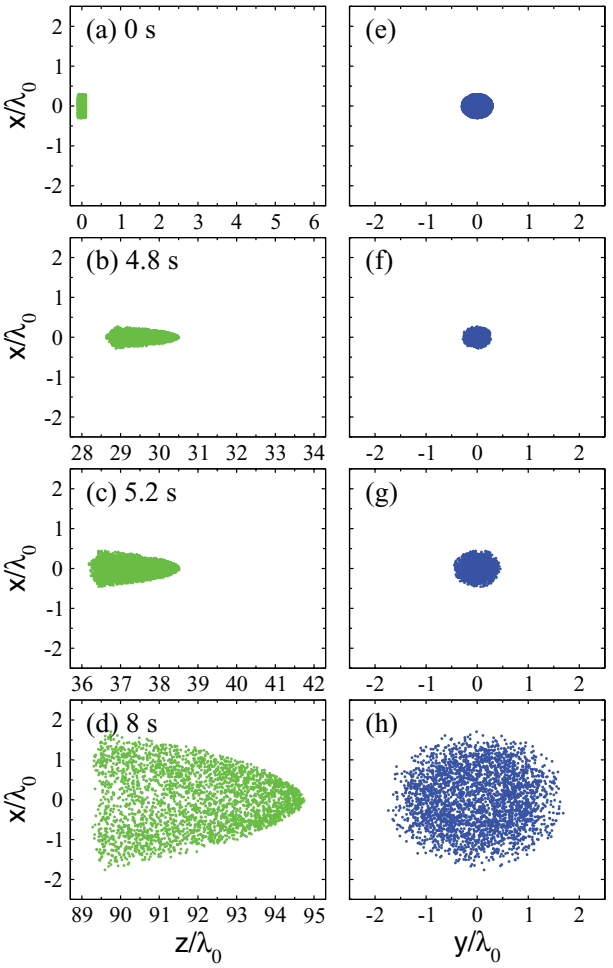

FIG. 8. (Color online) Same as Fig. 7, albeit for $b = 0.00577$.

$n_p \simeq 5.31 \times 10^{16}$ cm^{-3}, more than five orders of magnitude lower than the density of a typical solid. This fact is used as justification for neglecting the particle-particle interactions, in the many-particle calculations whose results will be presented in the present section.

Subsequent irradiation of the ensemble of protons by a radially polarized pulse will cause most of them to undergo oscillatory motion for a while followed by some gain in energy

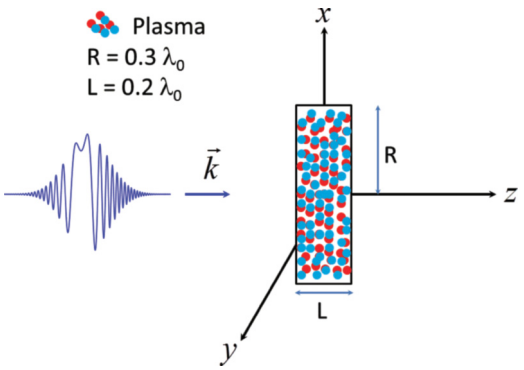

FIG. 9. (Color online) A schematic illustrating the initial conditions for a 2D underdense plasma prior to interaction with a chirped laser pulse incident upon it from the left.

and then a long excursion parallel to, or slightly deflected from, the z axis. Depending upon their initial positions, a small number of particles may end up traveling backwards. For a better picture of the motion of particles during and subsequent to irradiation with the pulse, 3D trajectories of 100 such particles are shown in Fig. 5 for the pulse parameters of Fig. 2 and $b = -0.006\,27$. In the figure, the trajectories appear to fill up a baseball-bat-shaped volume. For $\psi = 0$ and the pulse parameter set employed, the particles appear to be focused (pushed radially inward towards the z axis) by the radial electric field component E_r, while moving axially because of E_z. When E_r reverses direction, the focusing slows down and the particles get diffracted away from the z axis, and continue in straight line motion as they are left behind the pulse.

To gain more insight into the ensemble dynamics and understand the actual trajectories better, projection onto the xz plane of only small portions of the leftmost parts of four of the 3D trajectories shown in Fig. 5, are displayed in Fig. 6(a). The detailed picture in (b) confirms the earlier prediction: All four particles are pushed inward as they undergo axial oscillations, which subsequently grow in amplitude as the particles gain energy from the pulse. Finally the particles are swung forward along, or at a small angle to, the z axis.

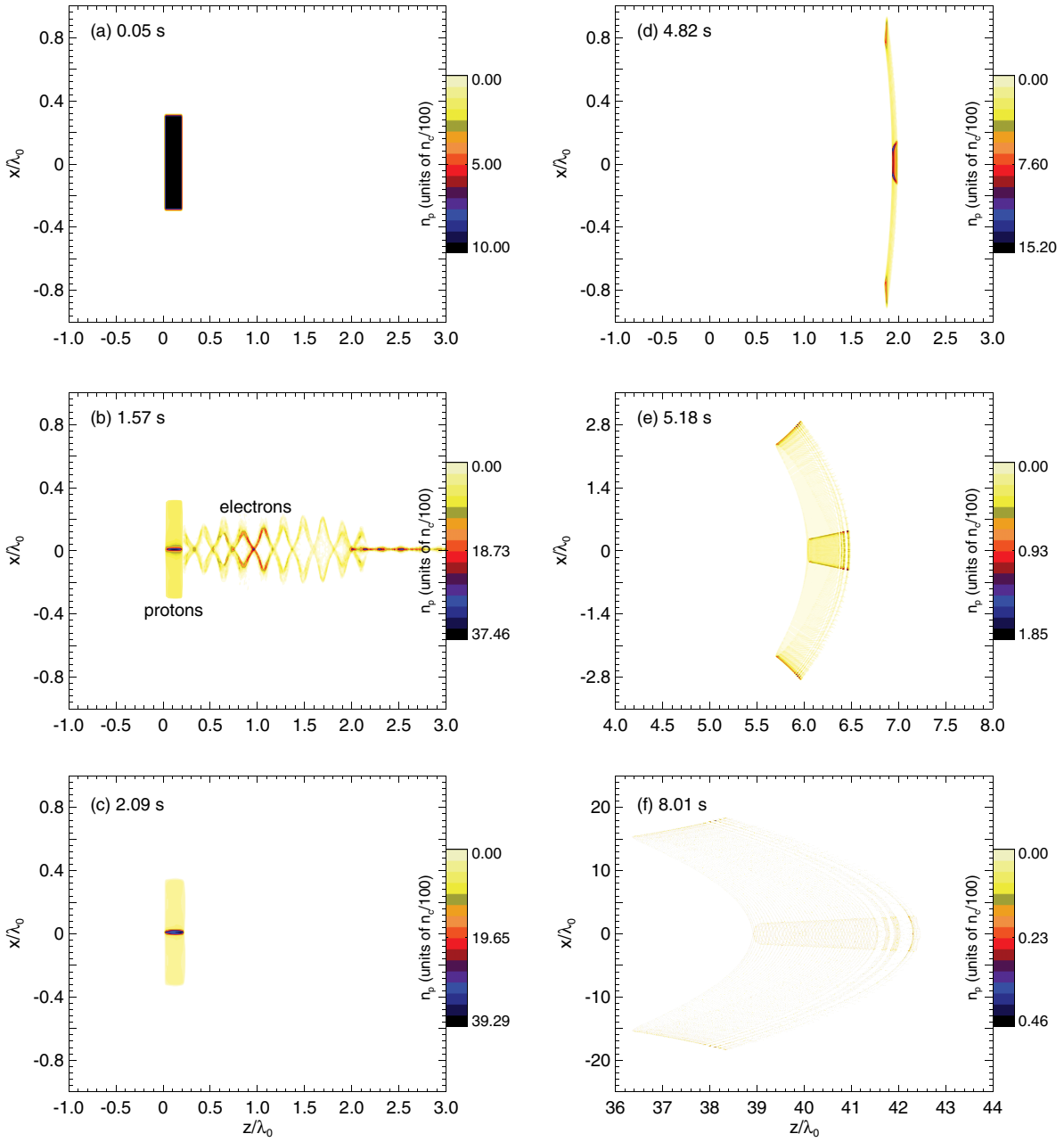

FIG. 10. (Color online) Density plots of the electron-proton plasma during interaction with a 1-PW, chirped, radially polarized laser pulse of duration $\tau = 150$ fs and dimensionless chirp parameter $b = -0.006\,39$. (a)–(f) are snapshots at instants corresponding to the values of η given on them in terms of $\sigma = \omega_0\tau/(2\sqrt{2\ln 2})$.

Turning now to evolution of the entire ensemble during interaction with the pulse, a series of four snapshots showing cross sections through it at four instants are shown in Fig. 7. The snapshots are taken at times corresponding to $\eta = 0, 4.8\sigma, 5.2\sigma$, and 8σ, respectively. Recall that a cross section of the initial ensemble at ($\eta = 0$) parallel to the xz plane is rectangular (length $0.6\lambda_0$ and width $0.2\lambda_0$), while one taken perpendicular to the z axis (parallel to the xy plane) is circular (of radius $0.3\lambda_0$). As can be seen in the panels of Figs. 7(a)–7(d) the rectangular cross section shrinks in height in going from Figs. 7(a) to 7(b) and shows expansion in Fig. 7(c). From Fig. 7(c) onwards, the cross section continues to expand, reaching a height of about $5\lambda_0$ at $\eta = 8\sigma$, the instant marking the end of interaction with the pulse. The far reaches (away from the z axis) of the distribution of particles in Fig. 7(d) appear to be less than in the middle (along z) due to the focusing alluded to above. This is confirmed by looking at the corresponding circular cross section in Fig. 7(h). The particle density close to the center of the circular cross section appears visually to be much higher than closer to its periphery. Evolution from the initial circle in Fig. 7(e) to that in Fig. 7(h) exhibits focusing followed by diffraction quite clearly. Here, too, the circular cross section reaches a diameter of nearly $5\lambda_0$, at the end of interaction with the laser pulse. Both panels of figures also demonstrate that the center of the distribution of accelerated particles seems to move along the z axis. As mentioned earlier, only those particles that start exactly on the z axis move subsequently along that axis, where $E_r = 0$. All other particles get diffracted off the z axis by a nonzero E_r.

Note that the center of the distribution moves, mostly along the z axis, a total distance of roughly $95\lambda_0$, during interaction with the pulse. Using the above data, the maximum deflection angle may be estimated to be $\sim 1.5^\circ$, with the z axis. The deflection angle, beyond the point corresponding to $\eta = 8\sigma$, depends crucially upon the velocity distribution of the particles of the ensemble at that point. Subsequently, deflection may be controlled, in principle, by electromagnetic means, which can also be used to steer the particle bunch to whatever target the application in question has. On the other hand, the average exit kinetic energy of the ensemble for the set of parameters used is $\bar{K}_{\rm exit} \simeq 236$ MeV, with a spread of $\simeq 0.8\%$.

The results displayed in Fig. 7 were for the case with chirp parameter $b = -0.006\,27$. The snapshot at the end of the interaction between the ensemble and the pulse shown in Fig. 7(d) exhibits a dense central *bulletlike* part around the z axis, surrounded by a conical part of markedly less density. The *bulletlike* feature, in particular, appears even more clearly in Fig. 8, which is a repeat of Fig. 7, albeit for the upchirp case of $b = 0.005\,77$. From Fig. 8(h) the maximum deflection of particles in the ensemble is about 1°, with the z axis. Finally, the average exit kinetic energy in this case is $\bar{K}_{\rm exit} \simeq 149$ MeV, and the spread in it is $\simeq 2\%$. Note that both examples agree roughly with the single-particle results, shown in Fig. 3.

V. PARTICLE-IN-CELL (PIC) SIMULATIONS

This section is devoted to the most realistic situation in which one lets a laser pulse, modeled most realistically using a Gaussian-beam-based representation, impinge upon an underdense hydrogen plasma (a preionized hydrogen gas jet or an expanding hydrogen cluster). The laser-plasma interaction, and evolution of the resulting particle dynamics, will be simulated using a 2D3V particle-in-cell model. A 2D distribution of dimensions $0.2\lambda_0$ (in the propagation direction of the pulse) by $0.6\lambda_0$ (in the direction of polarization) as shown in Fig. 9, will be considered here. The simulation box is divided into cells of dimensions (spatial resolution) $\Delta x = \Delta z = \lambda_0/100$ and temporal resolution $\Delta t = 0.005T$, where T is a laser field cycle. Each cell in the distribution is assumed to host 100 quasiparticles of each plasma component (ion or electron). The particle density is $n = 0.1 n_c$, for each particle species in the plasma, where $n_c = 1.1 \times 10^{21}$ cm^{-3} is the critical density corresponding to $\lambda_0 = 1\ \mu$m. The external laser fields are introduced as boundary conditions via the Cartesian components E_x, E_y, B_x, and B_y, determined from Eqs. (2)–(4), (16) and (17). The electromagnetic fields at all space-time grid points in the simulation box are then calculated by integration of Maxwell's equations self-consistently.

Density plots displaying evolution of the plasma during interaction with the pulse are shown in Fig. 10, for the case of pulse duration $\tau = 150$ fs and dimensionless parameter $b = -0.006\,39$. Shown are actually snapshots of the particle densities at instants corresponding to values of η given

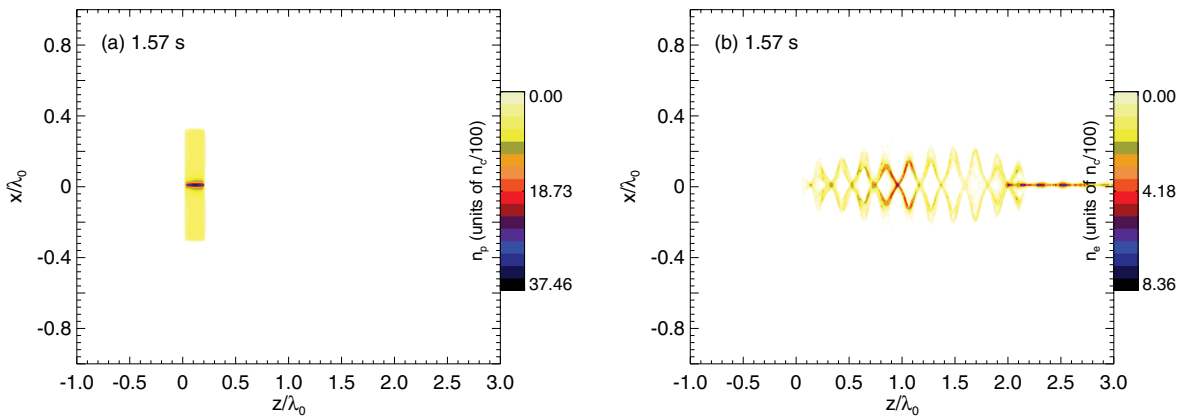

FIG. 11. (Color online) Density plots showing (a) the proton distribution, and (b) the electron distribution of Fig. 10(b) separately. In other words, (a) and (b) here, put together, yield Fig. 10(b).

on the figures in terms of the dimensionless variable $\sigma = \omega_0\tau/(2\sqrt{2\ln 2})$. The initial 2D plasma of protons and electrons is shown in Fig. 10(a). In Fig. 10(b) the electrons are shown being accelerated quickly away, axially by E_z and transversely by the much weaker E_r. As E_r oscillates, the electron transversal motion reverses direction accordingly. So, the little diffraction away from the z axis during interaction with an inward-pointing half cycle of E_r gives way to focusing around the pulse propagation axis during interaction with the next outward-pointing half cycle. To prove that the particles, shown in Fig. 10(b) following looplike trajectories about the z axis, are indeed the electrons, Fig. 11 has been produced, which shows the protons and electrons separately, in Figs. 11(a) and 11(b), respectively. The electrons disappear from any further density plots beyond (b) because they have been totally accelerated outside the ranges considered. Focusing of the protons begins to be evident also in Fig. 10(b), in which they advance axially a little, as well. Beyond Fig. 10(d), however, diffraction of the protons begins to show quite clearly, due to the Coulomb repulsion. Recall that $\eta = 8\sigma$ marks the end of interaction between the particles and pulse. The corresponding proton density plot, slightly after the particle-pulse interaction has ended, is shown in Fig. 10(f). There, the distribution shows a dense central part around the z axis, flanked by wings of much lower density. The wings are shown bent backwards because the particles in them experience a much weaker E_z than the ones closer to the z axis, get accelerated at a lower rate and fall behind the on-axis portions as the ensemble advances, as a

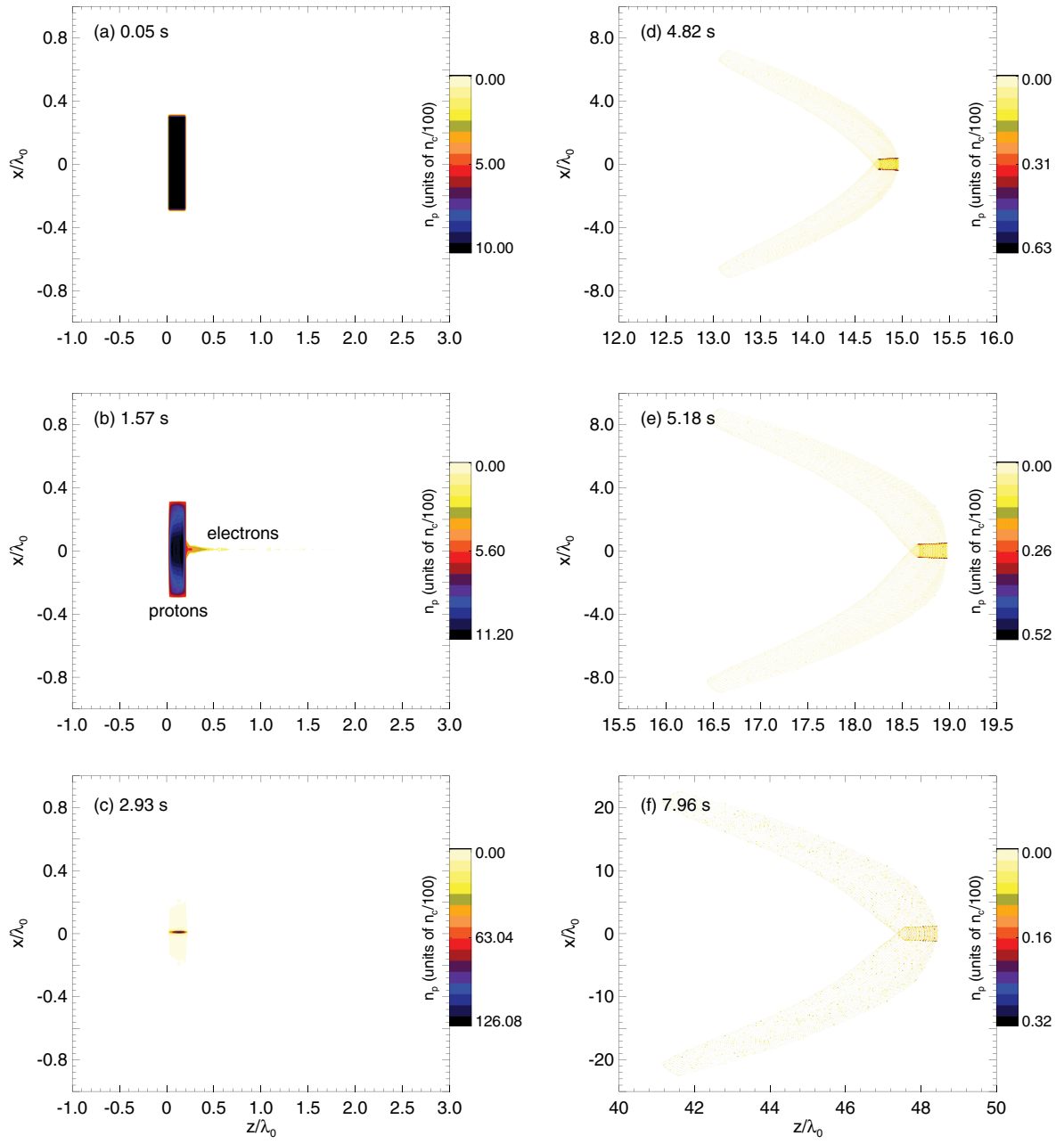

FIG. 12. (Color online) Same as Fig. 10, but for $b = 0.005\,75$.

whole, to the right. A rough estimate puts the total z excursion of the center of the distribution, during interaction, at $\simeq 40\lambda_0$, and the spatial spreading of the central dense part at $\simeq 6\lambda_0$.

Provided the low-density wings just described may be clipped away, the central high-density part can be aimed at a target for some application, such as ion therapy or in lithography. In fact, a more carefully chosen set of parameters may result in a *bulletlike* accelerated bunch of protons. An example of such a situation is displayed in Fig. 12. Even the electrons are accelerated in a very narrow bunch, as is clearly shown in Fig. 12(b). Towards the end of interaction with the pulse, Fig. 12(f) reveals that transverse spreading in the central maximum is $\simeq 4\lambda_0$, and that its center advances axially by $\simeq 48\lambda_0$.

A third set of parameters yields an even more pronounced *bulletlike* proton bunch, as shown in Fig. 13. The high-density central part, shown in Fig. 13(f), extends $\simeq 0.5\lambda_0$ transversely, and $\simeq 2\lambda_0$ axially. On the other hand, the low-density wings are too faint. The proton and electron distributions shown together in Fig. 13(b) are displayed separately in Fig. 14. Note that the electron distribution shown in Fig. 14(b) is much higher in density than, for example, its counterpart in Fig. 11. The presence of this high-density electron distribution, still after $\eta = 2.36\sigma$, exerts a stronger axial tug on the proton distribution, and plays a stronger role in ultimately forming the *bulletlike* structure shown so clearly in Figs. 13(c)–13(f).

The mean proton exit kinetic energies of the three cases investigated above by PIC simulation are collected in Table I. The energy spreads are all greater than the hoped for 1%, and reported above from the many-particle calculations. Note, however, that the averages have been calculated over all the

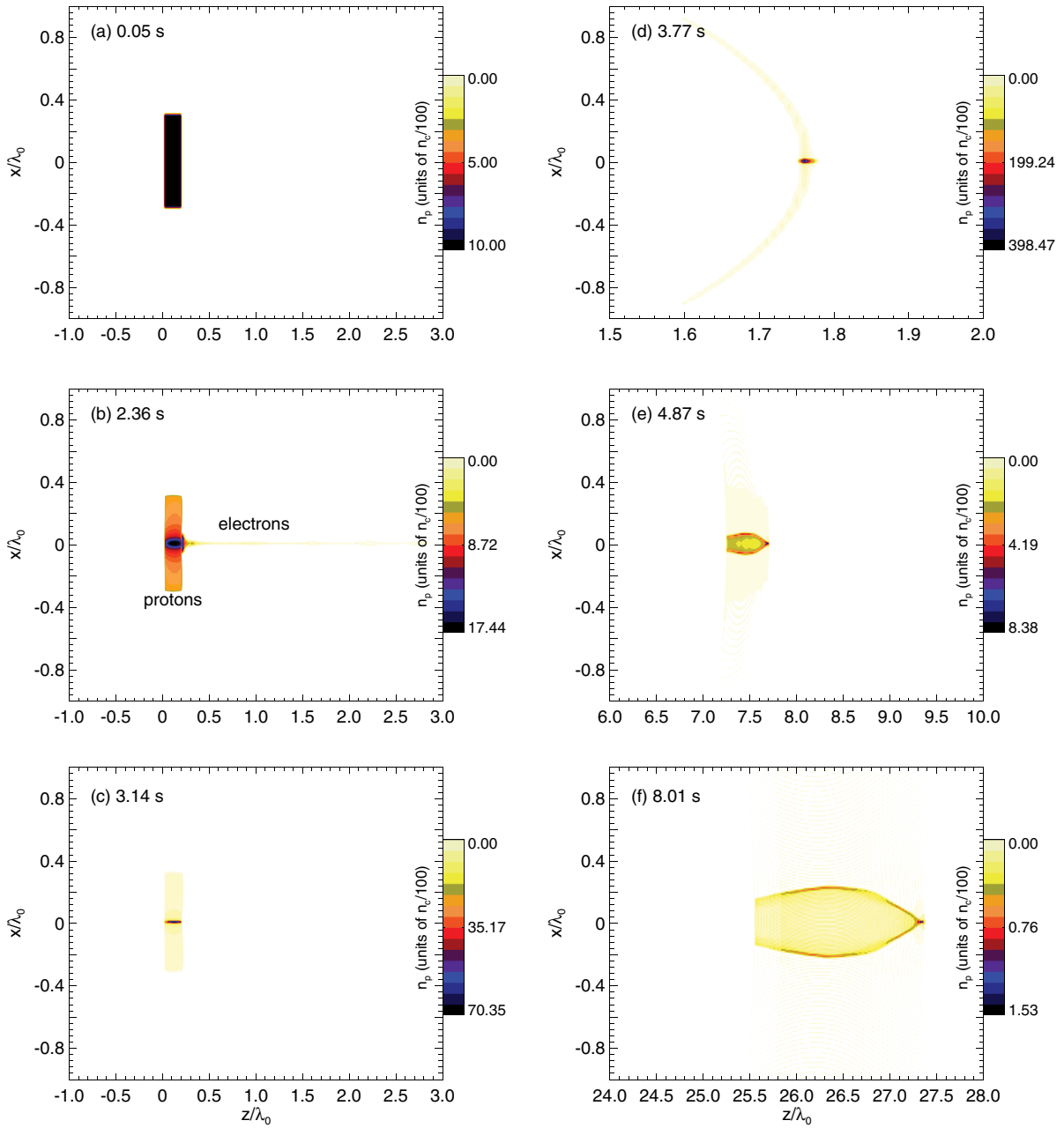

FIG. 13. (Color online) Same as Figs. 10 and 12, but for $b = 0.009\,25$, and $\tau = 100$ fs.

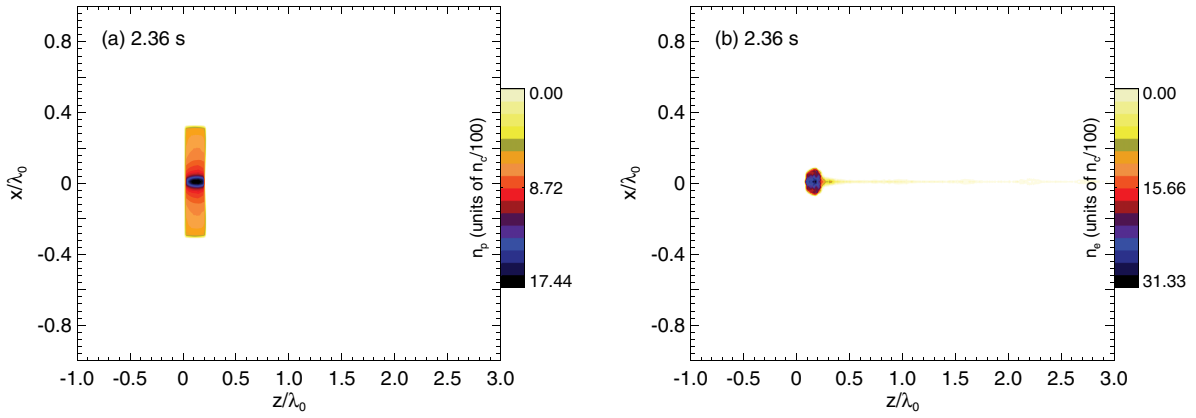

FIG. 14. (Color online) Density plots showing (a) the proton distribution, and (b) the electron distribution of Fig. 13(b) separately. In other words, (a) and (b) here, put together, yield Fig. 13(b).

particles in the sample, including the low-density wings. More importantly, the Coulomb repulsion has been neglected in the many-particle calculations. After the particles have been left behind the pulse, any deflection or spatial and energy spreading they undergo will only be due to mutual Coulomb repulsions, which can be controlled electromagnetically, from then on [52].

It may be thought that focusing and divergence in 2D and 3D are geometrically different, which may play a role over long distances compared to the wavelength. However, due to the cylindrical symmetry of the radially polarized laser fields, no appreciable discrepancy between the 2D and 3D results are to be expected. Furthermore, the noninteracting many particle simulations carried out in 3D show results similar to those of the 2D PIC calculations.

VI. DISCUSSION AND MAIN CONCLUSIONS

The aim of this work has been to identify conditions under which protons may be accelerated, using a 1-PW chirped radially polarized laser pulse, to energies making them suitable for various applications, especially ion therapy for which the minimum required energy is about 60 MeV [53–58]. A potential issue that may arise from using an underdense mass-limited target is its modification by a prepulse. Recent calculations, using linearly polarized fields of the same parameters, have shown that a prepulse does not change the target shape significantly (see end of Sec. IV in Ref. [30]). For issues concerning feasibility of the suggested acceleration mechanism, and target proposed, see [48]. Of greatest concern to readers of this paper is, understandably, the challenge of realizing a PW radially polarized laser beam. To the best of our knowledge, systems of much more modest powers have been used in laboratory experiments so far [19–22].

The goal has been pursued in single-particle calculations, supported by many-particle and particle-in-cell simulations. Sizes of the initial particle ensemble and simulation box have been chosen with the number of particles per bunch (10^7–10^{10}) needed for ion therapy in mind. It has been shown that a radially polarized pulse can accelerate the protons to less energies than can be done using a linearly polarized pulse of the same parameters and specifications. The good news is that the accelerated particle beam quality turns out to be better in the radially polarized case. An energy spread below 1% suits well the requirements of application in ion therapy, which has been demonstrated in this work, as can be seen by comparing the corresponding entries in Tables II and III. In achieving this beam quality, it has been shown that the role played by the radial component of the electric field E_r, for the choice of initial phase $\psi_0 = 0$, is crucial. Acceleration to the high energies obtained, and further collimated motion along the direction of pulse propagation, on the other hand, has been demonstrated to result from the energy carried by, and focused in, the axial component E_z.

The impressive beam quality, in energy and spatial spreading, is unfortunately not reflected by the PIC calculations. This is obviously due to taking the particle-particle Coulomb interactions into account in those calculations. Once the electrons have been accelerated away, the accelerated proton bunch can,

TABLE I. Mean proton exit kinetic energies and their spreads, after the end of interaction with a chirped 1-PW radially polarized laser pulse of duration τ and dimensionless chirp parameter b. The numbers have been calculated from the PIC simulations.

τ (fs)	b	$\bar{K}_{\rm exit}$ (MeV)	$\Delta K/\bar{K}_{\rm exit}$ (%)
150	− 0.006 39	281.8 ± 21.2	7.5
150	0.005 75	161.5 ± 10.7	6.6
100	0.009 25	108.2 ± 7.0	6.4

TABLE II. Mean proton exit kinetic energies $\bar{K}_{\rm exit}$ and the spread in them, calculated from subjecting an ensemble of 3000 protons, assumed noninteracting, to a 1-PW radially polarized laser pulse of duration τ, and waist radius $w_0 = \lambda_0$. The corresponding peak intensity is $I_0 \simeq 1.178 \times 10^{22}$ W/cm^2, and the chirp parameter values b^* are those that lead to a global maximum single-particle exit kinetic energy, in plots similar to that shown in Fig. 2.

τ (fs)	b^*	$\bar{K}_{\rm exit}$ (MeV)	$\Delta K/\bar{K}_{\rm exit}$ (%)
100	− 0.009 13	124.68 ± 1.05	0.84
150	− 0.006 27	236.03 ± 1.92	0.81
200	− 0.004 779 5	395.35 ± 15.40	3.89

TABLE III. Same as Table II, but for a linearly polarized laser pulse. The corresponding peak intensity is $I_0 \simeq 6.2012 \times 10^{22}$ W/cm^2, calculated from $I_0 = 2P_0[\pi w_0^2(1+\varepsilon^2/4+\varepsilon^4/8)]^{-1}$.

τ (fs)	b^*	$\bar{K}_{\rm exit}$ (MeV)	$\Delta K/\bar{K}_{\rm exit}$ (%)
100	0.009 14	334.12 ± 19.32	5.78
150	0.006 82	434.55 ± 30.53	7.03
200	0.005 835	496.08 ± 37.00	7.46

in principle, be collimated and guided electromagnetically to the target for application.

Earlier work [31] has demonstrated that, for unchirped laser acceleration of protons to the levels achieved here, a laser system of 10 PW or more is needed and that such a system ought to be focused to a subwavelength waist radius, thus sending the intensity beyond 10^{23} W/cm^2. In effect, calculations in the present work, employing chirped laser pulses, have shown that the same goal can be achieved (employing a chirped pulse, instead) by power and intensity levels at least one order of magnitude lower. Besides, the need to focus to subwavelength waist radii has been avoided altogether.

It has been shown elsewhere [31], too, that the energy gain by an ion from interaction with an unchirped laser pulse scales linearly with the input power. This seems to hold approximately true when the pulse is chirped. Detailed, many-particle calculations with 150-fs pulses of input powers of 1, 0.1, 0.01, and 0.001 PW have shown that protons may be accelerated to the mean kinetic energies of 236 ± 2, 12.1 ± 0.1, 1.06 ± 0.03, and 0.102 ± 0.003 MeV, respectively. For all of these results the dimensionless chirp parameter has been $b^* = -0.006\,27$, and the pulse has been focused to $w_0 = \lambda_0$.

One final point to consider concerns the radiation reaction effects that may affect the acceleration process using the laser intensity levels employed in our work. Note first that, due to the early separation of electrons from ions [see Figs. 10(b), 12(b), and 13(b)] and the subsequent direct acceleration of the ions by the laser fields, radiation reaction effects are not expected to influence the ion spectra. Furthermore, in Ref. [59] it has been demonstrated that, even for overdense targets where electron-ion interactions play a major role, radiation reaction effects start first to significantly influence the ion spectra at peak laser intensities in excess of 10^{23} W/cm^2. Such peak intensities are one order of magnitude higher than the peak intensities used in the present work.

ACKNOWLEDGMENTS

Y.I.S. is supported by the Arab Fund for Economic and Social Development (State of Kuwait) through a Distinguished Scholar Award.

[1] S. Quabis, R. Dorn, M. Eberler, O. Glockl, and G. Leuchs, Opt. Commun. **179**, 1 (2000).
[2] K. Youngworth and T. Brown, Opt. Express **7**, 77 (2000).
[3] S. Quabis, R. Dorn, M. Eberler, O. Glockl, and G. Leuchs, Appl. Phys. B **72**, 109 (2001).
[4] R. Dorn, S. Quabis, and G. Leuchs, Phys. Rev. Lett. **91**, 233901 (2003).
[5] J. Tauer, F. Orban, H. Kofler, A. B. Fedotov, I. V. Fedotov, V. P. Mitrokhin, A. M. Zheltikov, and E. Wintner, Laser Phys. Lett. **4**, 444 (2007).
[6] L. Novotny, M. R. Beversluis, K. S. Youngworth, and T. G. Brown, Phys. Rev. Lett. **86**, 5251 (2001).
[7] C. J. R. Sheppard and M. Gu, J. Mod. Opt. **40**, 1631 (1993); C. J. R. Sheppard and M. Martinez-Corral, Opt. Lett. **33**, 476 (2008); C. J. R. Sheppard and E. Y. S. Yew, *ibid*. **33**, 497 (2008); C. J. R. Sheppard and S. Rehman, Appl. Opt. **50**, 4463 (2011).
[8] N. Davidson and N. Bokor, Opt. Lett. **29**, 1318 (2004).
[9] Y. I. Salamin, Opt. Lett. **32**, 3462 (2007).
[10] Y. I. Salamin, Phys. Rev. A **82**, 013823 (2010).
[11] Y. I. Salamin, Phys. Lett. A **374**, 4950 (2010).
[12] Y. I. Salamin, Phys. Lett. A **375**, 795 (2011).
[13] Y. I. Salamin, Phys. Rev. ST-AB **14**, 071302 (2011).
[14] S. C. Tidwell, D. H. Ford, and W. D. Kimura, Appl. Opt. **29**, 2234 (1990).
[15] Y. Kozawa and S. Sato, Opt. Lett. **30**, 3063 (2005).
[16] W. J. Lai, B. C. Lim, P. B. Phua, K. S. Tiaw, H. H. Teo, and M. H. Hong, Opt. Express **16**, 15694 (2008).
[17] G. Machavariani, Y. Lumer, I. Moshe, A. Meir, and S. Jackel, Opt. Lett. **32**, 1468 (2007).
[18] C. F. Phelan, J. F. Donegan, and J. G. Lunney, Opt. Express **19**, 21793 (2011).
[19] M. A. Ahmed, J. Schulz, A. Voss, O. Parriaux, J.-C. Pommier, and T. Graf, Opt. Lett. **32**, 1824 (2007).
[20] M. A. Ahmed, M. Haefner, M. Vogel, C. Pruss, A. Voss, W. Osten, and T. Graf1, Opt. Express **19**, 5093 (2011).
[21] W. D. Kimura, G. H. Kim, R. D. Romea, L. C. Steinhauer, I. V. Pogorelsky, K. P. Kusche, R. C. Fernow, X. Wang, and Y. Liu, Phys. Rev. Lett. **74**, 546 (1995).
[22] Y. Liu, D. Cline, and P. He, Nucl. Instrum. Methods Phys. Res., Sect. A **424**, 296 (1999).
[23] K. P. Singh, Appl. Phys. Lett. **87**, 254102 (2005); K. P. Singh and V. Sajal, Phys. Plasmas **16**, 043113 (2009); K. P. Singh and M. Kumar, Phys. Rev. ST Accel. Beams **14**, 030401 (2011).
[24] D. N. Gupta and H. Suk, Phys. Plasmas **13**, 044507 (2006); D. N. Gupta, H. Suk, and M. S. Hur, Appl. Phys. Lett. **91**, 211101 (2007).
[25] F. Sohbatzadeh, S. Mirzanejhad, and M. Ghasemi, Phys. Plasmas **13**, 123108 (2006).
[26] F. Sohbatzadeh, S. Mirzanejhad, and H. Aku, Phys. Plasmas **16**, 023106 (2009).
[27] F. Sohbatzadeh and H. Aku, J. Plasma Phys. **77**, 39 (2011).
[28] J.-X. Li, W.-P. Zang, and J.-G. Tian, Appl. Phys. Lett. **96**, 031103 (2010).
[29] B. J. Galow, Y. I. Salamin, T. V. Liseykina, Z. Harman, and C. H. Keitel, Phys. Rev. Lett. **107**, 185002 (2011).
[30] Y. I. Salamin, J.-X. Li, B. J. Galow, Z. Harman, and C. H. Keitel, Phys. Rev. A **85**, 063831 (2012).

[31] Z. Harman, Y. I. Salamin, B. J. Galow, and C. H. Keitel, Phys. Rev. A **84**, 053814 (2011).
[32] M. Borghesi, J. Fuchs, S. V. Bulanov, A. J. Mackinnon, P. K. Patel, and M. Roth, Fusion Sci. Technol. **49**, 412 (2006).
[33] E. L. Clark *et al*., Phys. Rev. Lett. **84**, 670 (2000).
[34] R. A. Snavely *et al*., Phys. Rev. Lett. **85**, 2945 (2000).
[35] S. C. Wilks *et al*., Phys. Plasmas **8**, 542 (2001).
[36] A. Macchi, F. Cattani, T. V. Liseykina, and F. Cornolti, Phys. Rev. Lett. **94**, 165003 (2005).
[37] J. Badziak, Opto-electr. Rev. **15**, 1 (2007).
[38] J. Fuchs *et al*., Nature Phys. **2**, 48 (2006); L. Robson *et al*., *ibid*. **3**, 58 (2007).
[39] See M. Passoni, L. Bertagna, and A. Zani, New J. Phys. **12**, 045012 (2010), and references therein.
[40] A. P. L. Robinson *et al*., New J. Phys. **10**, 013021 (2008).
[41] B. Qiao, M. Zepf, M. Borghesi, and M. Geissler, Phys. Rev. Lett. **102**, 145002 (2009).
[42] A. Macchi, S. Veghini, T. V. Liseykina, and F. Pegoraro, New J. Phys. **12**, 045013 (2010).
[43] V. T. Tikhonchuk, Nucl. Instrum. Methods A **620**, 1 (2010).
[44] C. A. J. Palmer *et al*., Phys. Rev. Lett. **106**, 014801 (2011).
[45] S. TerAvetisyan, M. Schnurer, P. V. Nickles, M. Kalashnikov, E. Risse, T. Sokollik, W. Sandner, A. Andreev, and V. Tikhonchuk, Phys. Rev. Lett. **96**, 145006 (2006).
[46] B. Ramakrishna *et al*., Phys. Plasmas **17**, 083113 (2010).
[47] S. Buffechoux *et al*., Phys. Rev. Lett. **105**, 015005 (2010).
[48] F. Peano *et al*., Phys. Plasmas **14**, 056704 (2007).
[49] F. Peano, J. Vieira, R. A. Fonseca, R. Mulas, G. Coppa, and L. O. Silva, IEEE Trans. Plasma Sci. **36**, 1857 (2008).
[50] Y. I. Salamin, New J. Phys. **8**, 133 (2006).
[51] Y. I. Salamin, Phys. Rev. A **73**, 043402 (2006).
[52] M. Schollmeier *et al*., Phys. Rev. Lett. **101**, 055004 (2008).
[53] S. E. Combs *et al*., Cancer **115**, 1348 (2009).
[54] D. Schardt, T. Elsässer, and D. Schulz-Ertner, Rev. Mod. Phys. **82**, 383 (2010).
[55] S. V. Bulanov and S. V. Khoroshkov, Plasma Phys. Rep. **28**, 453 (2002); E. Fourkal *et al*., Med. Phys. **30**, 1660 (2003); V. Malka *et al*., *ibid*. **31**, 1587 (2004); J. Fuchs *et al*., Nature Phys. **2**, 48 (2006).
[56] S. Fritzler, K. Ta Phuoc, V. Malka, A. Rousse, and E. Lefebvre, Appl. Phys. Lett. **83**, 3039 (2003).
[57] X. Y. Peng, J. Zhang, J. Zheng, Z. M. Sheng, M. H. Xu, Z. Y. Zheng, T. J. Liang, Y. T. Li, Q. L. Dong, X. H. Yuan, Y. J. Li, and H. M. Li, Phys. Rev. E **74**, 036405 (2006).
[58] O. Jäkel, D. Schulz-Ertner, C. P. Karger, P. Heeg, and J. Debus, Nucl. Instrum. Methods Phys. Res., Sect. B **241**, 717 (2005); O. Jäkel, M. Krämer, C. P. Karger, and J. Debus, Phys. Med. Biol. **46**, 1101 (2001); http://www.wanjiehospital.com/proton/program.htm.
[59] M. Tamburini, F. Pegoraro, A. Di Piazza, C. H. Keitel, and A. Macchi, New J. Phys. **12**, 123005 (2010).